Powder Technology 460 (2025) 121048

Contents lists available at ScienceDirect

Powder Technology

journal homepage: www.journals.elsevier.com/powder-technology

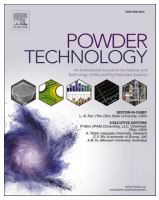

Simulation-based characterization of alginate aerogel packed bed compaction via DEM-BPM

C.L. Alves [a,*], L. Gibowsky [b], B. Schroeter [b], I. Smirnova [b], S. Heinrich [a]

[a] Institute of Solids Process Engineering and Particle Technology, Hamburg University of Technology (TUHH), 21073 Hamburg, Germany
[b] Institute for Thermal Separation Processes, Hamburg University of Technology (TUHH), 21073 Hamburg, Germany

HIGHLIGHTS

- Mechanical and simulation characterization aerogels under uniaxial compaction.
- DEM-BPM model accurately simulates single aerogel and packed beds of aerogels.
- Strong correlation between experiments and simulations.
- Proposed optimization methodology enhances aerogel production efficiency.
- High potential to extend the simulation model to intermediate stages as hydrogels and alcogels.

GRAPHICAL ABSTRACT

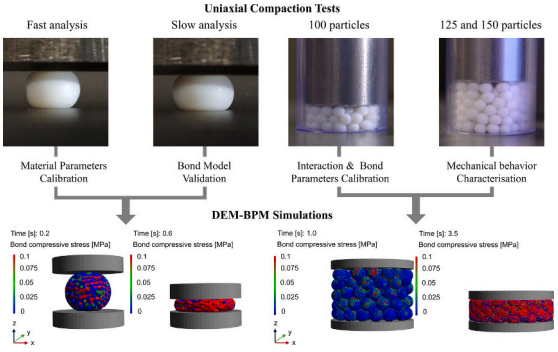

ARTICLE INFO

Keywords:
Aerogel
Mechanical charaterization
DEM-BPM simulation
Optimized simulation

ABSTRACT

The global demand for aerogels is constantly growing, thus, optimizing and scaling up the production processes have become increasingly important in the last decade. The utilization of millimeter-sized aerogel particles for such purposes is typically preferred due to inherent advantages in handling and production compared to other geometries. The production of these particles is most commonly accomplished using a particle packed bed (autoclave). This process presents, however, several challenges, including the impact of mechanical loads on the quality of the product. Therefore, this work focuses on deepening the understanding of mechanical properties and deformation mechanisms of aerogel particles in packed beds under uniaxial compaction. The investigated alginate aerogel particles are characterized by a spherical shape (circularity of 0.96), a specific surface area of ~352 m^2/g, an average diameter of ~3.3 mm, and a bulk density of ~0.05 g/cm^3. In addition, this study extends a DEM-BPM model to capture the mechanical deformation of biopolymer aerogels, both as individual particles and within packed beds. The simulations were calibrated and validated using experimental data from uniaxial compaction tests. An optimization methodology was implemented to reduce reliance on traditional trial-and-error methods and improve the model's accuracy. The results demonstrate that the proposed DEM-BPM model effectively replicates the mechanical behavior of alginate aerogels, showing strong agreement between experimental data and minimal deviations for both single particles and packed beds ($R^2 \geq 0.93$). This model serves as a promising tool for gaining deeper insights into the mechanical properties of aerogels and improving production

* Corresponding author.
E-mail address: carine.lourenco.alves@tuhh.de (C.L. Alves).

https://doi.org/10.1016/j.powtec.2025.121048
Received 31 January 2025; Received in revised form 17 April 2025; Accepted 18 April 2025
Available online 18 April 2025

efficiency. Additionally, the DEM-BPM model can be expanded to incorporate intermediate products, such as hydrogels and alcogels, enabling process optimization at every stage of aerogel manufacturing.

1. Introduction

Aerogels are highly porous solid materials characterized by their predominantly mesoporous architecture (pore diameter in the range of 2–50 nm). These unique materials exhibit extremely low densities (0.003 to 0.15 kg/m^3), high porosities (up to 99 %), and specific surface areas reaching up to 1000 m^2/g. These attributes can contribute to low thermal conductivities [1,2]. Consequently, aerogels have attracted significant research interest over the past decade, being used in a wide array of applications, including catalysts [3], thermal and acoustic insulation [4], pharmaceutical carriers [5], adsorption and absorption matrices, and medical applications [6]. Due to their innovative potential, aerogels were recognized by the IUPAC as one of the top 10 emerging technologies in 2022 [7].

Aerogel synthesis typically involves a three-step process: 1) gel formation in an aqueous solution, involving either a chemical reaction or physical crosslinking; 2) solvent exchange, wherein water is replaced by an organic solvent such as ethanol; 3) supercritical drying and 4) depressurization. Fig. 1 Shows the schematic production of gel particles in packed beds.

During the drying phase, the extraction of the organic solvent using supercritical CO_2 takes place at pressures of 120 to 140 bar and temperatures exceeding 40 °C [8]. This process is fundamentally akin to the well-known supercritical fluid extraction (SFE) of valuable substances from solid materials, such as natural oils and aromatic compounds [9,10]. In aerogel production, supercritical CO_2 is employed to extract residual ethanol from the pore structure of the alcogel. The supercritical state of the CO_2-ethanol mixture prevents the formation of phase boundaries, thereby eliminating capillary forces that could otherwise damage the mesoporous structure [2,11]. Upon depressurization and opening of the autoclave, the CO_2 within the pores is replaced by air, yielding the final aerogel product.

Aerogels can be fabricated in various forms, including monoliths, plates, and particles. Spherical particles exhibit several advantages over other geometries, including improved handling, enhanced transportability, and reduced processing times due to diminished diffusion limitations. While the drying of millimeter-sized individual particles occurs within minutes, monoliths or plates require several hours [12,13]. This is one of the reasons why current industrial practices usually favor batch-wise supercritical drying of particle packed beds using CO_2. Due to the substantial growth of possible applications over the last decade [11,14,15], there is a growing global demand for aerogels, particularly in particle and powder forms.

To scale up the process in particle packed beds, it is crucial to increase the volume of the solvent exchange vessel and autoclave. This adjustment aims to achieve a higher yield per batch while simultaneously reducing production costs. A critical aspect of this optimization is the implementation of a higher length-to-diameter (L/D) ratio in the autoclave design, which minimizes both the spatial footprint and production/equipment costs. However, this design introduces several challenges, particularly concerning the (mechanical) forces acting on packed beds, which can lead to deformation and densification of the particles within the bed, creating significant operational issues. The forces contributing to these challenges arise predominantly during the solvent exchange and supercritical drying and can be categorized as follows: a) hydrodynamic forces, induced by fluid flow and the corresponding pressure drop within the bed; b) gravitational forces, the weight of the particles, particularly pronounced in the lower section of the packed bed; c) wall friction. The resulting mechanical load often leads to the partial destruction of the macroscopic particle shape. At the same time, changes in the microstructure can occur, as indicated by a shift of the pore size distribution to smaller pores [16,17]. These changes can influence the mass and heat transport properties of the gels. Under controlled conditions, this can offer advantages such as reduced thermal conductivity or increased transparency [17,18]. However, the correlation between particle deformation and microstructure has not yet been investigated in the context of aerogels in particle beds.

To address a part of this gap, the present study focuses on the deformation mechanisms occurring during the batchwise production of particle packed beds for aerogels — a topic that has not been explored in depth. For simplification, this study concentrates exclusively on the behavior of aerogels under static conditions (without the influence of liquids such as ethanol or water). To replicate the external forces acting on aerogel particles, uniaxial compaction tests are performed. Although there are already several studies on the mechanical properties of biopolymer aerogels, these have so far focused exclusively on aerogel monoliths, for example, those based on cellulose or alginate [19–21]. Therefore, this work aims to investigate and model the mechanical response of biopolymer aerogel particles under load via DEM-BPM simulations to gain a deeper understanding of the underlying mechanisms. This study focuses exclusively on biopolymer aerogels, which offer several advantages compared to conventional silica aerogels. These include the production from renewable, biodegradable raw materials (e.g., cellulose, chitosan, alginate), as well as non-toxicity and biocompatibility, enabling their use in medical and food applications. In addition, biopolymer aerogels exhibit enhanced mechanical stability, a

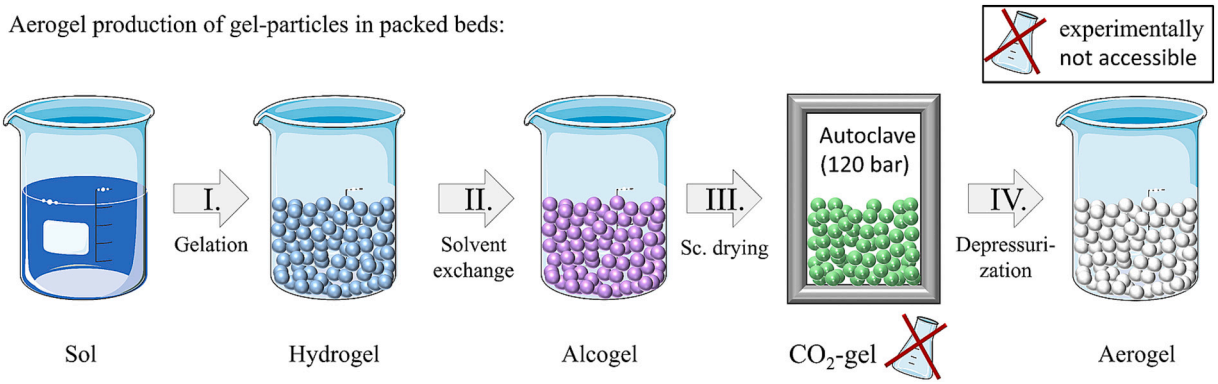

Fig. 1. Production process of aerogels, the different colors represent the variation of solvents: 1) water (blue), 2) ethanol (purple), 3) CO_2 (green), and 4) air (white). (For interpretation of the references to colour in this figure legend, the reader is referred to the web version of this article.)

critical factor for scaling up the production processes [14]. The framework of the work is illustrated in Fig. 2. A video showing the process of a packed bed compression at the Texture Analyzer is provided in the Supporting Information: (See Fig. S1.)

The initial phase of this study focuses on analyzing the compaction behavior of individual alginate aerogel particles, serving as a calibration step for DEM-BPM simulations. Subsequently, the study examines the behavior of these particles within packed beds containing 100 to 150 particles, a scale that is computationally feasible for the simulations.

A DEM-BPM-based model used for examining the mechanical behavior of aerogels has been proposed by Dosta et al. [21]. The Bonded-Particle Method (BPM) has been formulated as an extension of the discrete element method (DEM) for the modeling of granular materials [22]. A material modeled by the BPM is depicted as a collection of discrete primary particles interconnected by solid or liquid bonds. Each bond links two primary particles, and depending on the relative motion of the connected particles, forces and moments arise within the bond. These forces and moments ultimately act on primary particles, resulting in their translational and rotational motion. At each time step, supplementary breakage criteria are evaluated. Upon fulfilling any criterion, the bond is destroyed and eliminated from the simulation domain. In recent years, BPM has been extensively utilized for modeling various materials, including glass agglomerates, concrete [23,24], sandstone [25], and porcelain [26]. The proposed model includes three primary components: the structural model to depict the internal material architecture, the functional model to elucidate the mechanical behavior of individual components, and the model parameters that must be calibrated to the experimental data.

The elasto-plastic Bonded Particle Model (BPM) from Dosta et al. [21] successfully replicated the macro-scale mechanical behavior of the studied aerogel monoliths with varying crosslinking degrees, demonstrating only moderate deviations. This highlights the potential of the developed DEM-BPM model to effectively simulate aerogel particles with high efficiency, providing valuable insights into the underlying mechanisms. Our work is grounded in this research. In our study, we refine the model by incorporating experimental observations and applying it to single particles and particle beds, enabling a more accurate representation of their mechanical behavior and providing deeper insights into the deformation mechanisms that arise during the batch-wise production of particle-packed aerogel beds—a topic that remains underexplored in the literature.

2. Materials and method

2.1. Experiments

2.1.1. Sample preparation

The production of aerogels begins with the preparation of an aqueous biopolymer solution using alginate (IFF Division Pharma Solutions) with a G/M ratio of 0.57 and a concentration of 2 wt%. The gelation of this solution was carried out by using the dripping method to achieve particles of approximately 3 mm [27]. The dripping process involved extruding the biopolymer solution through a syringe (referred to as a "spider") equipped with blunt needles at the outlet with an inner diameter of 0.26 mm. The aqueous alginate solution was dropwise added into a 2 wt% $CaCl_2$ aqueous solution (Carl Roth GmbH & Co. KG) under continuous stirring at a distance of 12 cm. As a result, spherical hydrogel particles were obtained and subjected overnight in the $CaCl_2$ solution to ensure complete gelation. The particles are then counted manually 3 times in the hydrogel state for the packed bed analyses and the average weight is determined. The corresponding weights for 100, 125 and 150 particles are used as reference weights for the remaining 17 samples. Subsequently, the hydrogels undergo a direct solvent exchange with 99.9 wt% anhydrous ethanol (EtOH, Carl Roth GmbH & Co. KG) at room temperature. This procedure was repeated until the ethanol concentration reached at least 97 wt% for the resulting alcogels, as confirmed by density measurements (Anton Paar, DMA 4500 M). To prevent any deformation prior to analysis in the Texture Analyzer, the direct solvent exchange was carried out in filter paper bags containing the particles. The process of supercritical drying (extraction of ethanol

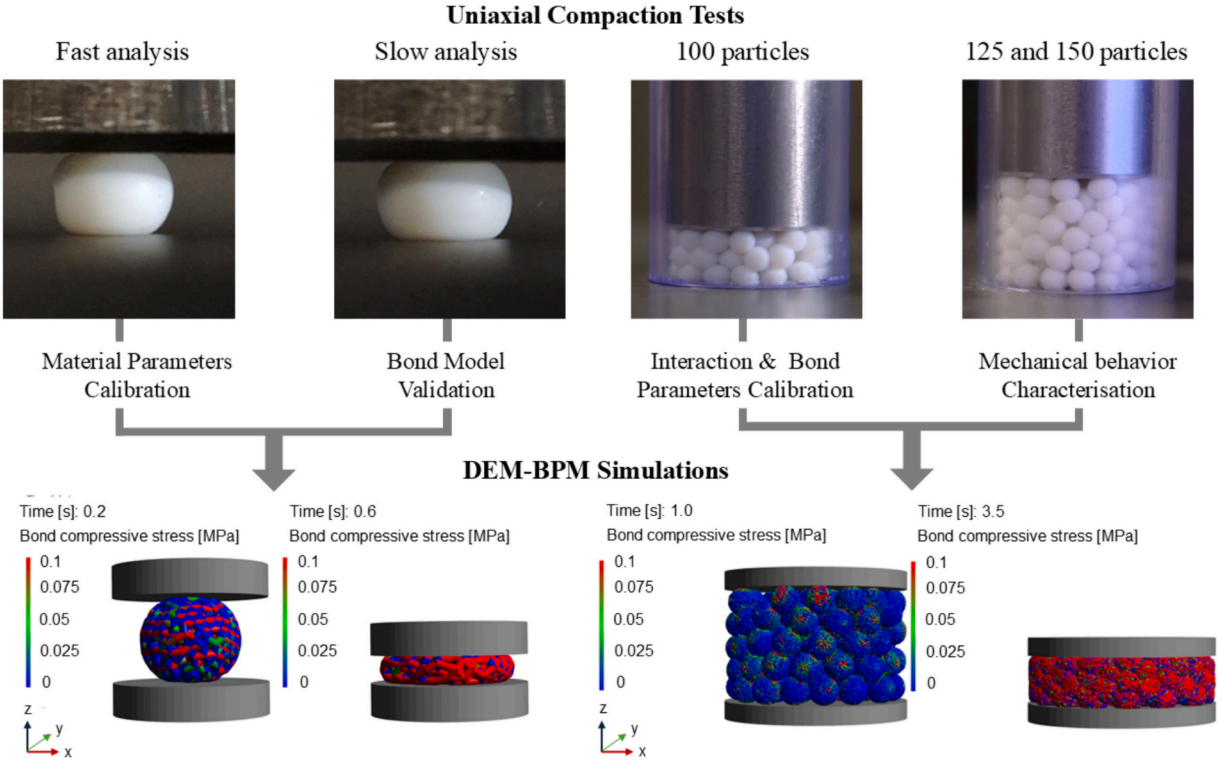

Fig. 2. Framework of the developed study.

with supercritical CO_2) was conducted in a 4 L autoclave under the operating conditions of 120 bar and 60 °C for a total duration of 120 min. The autoclave was filled with alcogel particles sealed in filter bags to prevent initial deformation. Supercritical CO_2 was continuously added to the autoclave with a constant flow rate of 350 g/min. After the depressurization (2 bar min^{-1}), all aerogel particles were collected and stored in sealed cups in a desiccator prior to analysis.

2.1.2. Characterization of aerogels

The diameter and circularity of the aerogel particles were established through image analysis of five distinct photos containing 10 aerogels and a ruler, using ImageJ for the process.

The solid bulk density was determined using sample volumes of 11.5 cm^3. The mass of each sample was measured with high precision using an analytical scale (Excellence Plus XP, Mettler Toledo), ensuring accurate and reliable density evaluation.

Scanning electron microscopy (SEM, Zeiss Supra VP55, Jena, Germany) was used to characterize the inner pore structure of aerogel particles. In order to analyze the interior of the particles, the sample was first cut in half, after which small pieces were taken from the center. All samples were sputtered with a 6 mm thin layer of gold (Sputter Coater SCD 050, BAL-TEC). The SEM picture was taken under a high vacuum using an Inlens detector (accelerating voltage = 3 kV, magnification = 50,000×, and working distance = 5.8 mm).

The mass specific surface area (S_m), mesopore size distribution, mean pore diameter ($d_{p,mean}$), and mesopore volume (V_{meso}) of aerogel particles were determined via low-temperature N2 adsorption-desorption analysis (Nova 3000e Surface Area Analyzer, Quantachrome Instruments). A sample weight of approx. 20 mg was used in each case and degassed under vacuum (60 °C and 6 h) prior to the measurement. All determinations were carried out in triplicate. While the BJH (Barrett-Joyner-Halenda) method was used to determine V_{meso} and $d_{p,mean}$, the specific surface area S_m was calculated based on the BET (Brunauer-Emmett-Teller) method. The corresponding BET-plots, isotherms with Type IV hysteresis according to the IUPAC classification [30], and pore size distributions of all three measurements are displayed in Fig. S1.

PowerPoint 2016 was used to optimize the brightness and contrast of the SEM images and photographs.

All mechanical experiments were performed as uniaxial compactions using a Texture Analyzer device (Stable Micro Systems Ltd., Surrey, United Kingdom). A video illustrating the compaction measurements is provided in S2. The device offers a force resolution of 0.1 g and a displacement resolution of 0.001 mm. The experiments included both individual particles and particle beds containing 100, 125, and 150 particles. For single-particle investigations, the probe velocity was set to 0.3 mm/s and 3 mm/s to evaluate the model's ability to replicate the mechanical behavior of aerogels under varying compaction velocities. Particle bed experiments were conducted at a probe velocity of 3 mm/s. The stopping conditions were defined as reaching a force of 100 N for single particles and 500 N for packed beds. A trigger value of 0 N was defined to indicate the initiation of the measurement. To precisely identify the actual starting point of the compression measurement, a Python script was used to calculate the running average of the recorded force values. The script detected the moment at which a continuous increase in force occurred, and all data points recorded prior to this point were excluded from further analysis. Each compaction analysis setting was repeated 20 times to ensure statistically significant results. While the analysis of the individual particles is limited to the force-displacement curve due to the geometric conditions (constantly changing contact surface of probe and gel sphere), the strain-stress curves were calculated for the packed beds.

2.2. Numerical background

In the BPM, aerogels are represented as agglomerates formed by small, ideally spherical primary particles interconnected by solid bonds. The bonds are modeled as massless cylindrical entities capable of transmitting forces and moments. In the general formulation of BPM, particles may interact when in direct contact and through the bonds that connect them. Both interactions are evaluated independently and may occur simultaneously between the same pair of particles. However, in this work, the interaction scheme is modified so that particle-particle contact forces are not calculated between primary particles directly connected by a bond. This modification is intended to provide a more realistic representation of the nonlinear elasto-plastic mechanical behavior of the aerogel bodies. After the bond breakage, the corresponding particles can reengage into direct contact, and the associated contact forces are calculated as usual. All interactions between particles not directly connected by bonds are treated according to the selected contact force models.

The BPM serves as a mathematical framework designed to depict real-world entities and simulate their behaviors. The model can be divided into three main components:

- structural model: encompassing spatial material distribution, positions and radii of primary particles, and the connections between them, including bond radii;
- functional model: detailing the functional dependencies that describe the forces and moments acting within the bonds and among primary particles;
- model parameters: including calibrated parameters that characterize plasticity, softening, and related aspects.

All simulations have been performed in the DEM modeling framework MUSEN [39].

2.2.1. Structural model

The structural model is generated in two consequent stages, including the creation of primary particles and solid bonds. In the first stage, a packing of primary particles is created using a force-biased algorithm. A generation domain is a sphere whose size is determined through image analysis of the aerogels. First, particles are placed randomly within the domain, and then, according to the calculated repelling forces, they are iteratively moved to avoid interparticle overlaps. The radius of all primary particles is 152.5 μm. In the second stage, bonds are generated between all pairs of particles whose surface distances range from −0.1 (overlapping) to 50 μm. All bonds have the same radius of 122.5 μm.

Before the primary analysis, the particle and bond radii and the maximum bond lengths were systematically varied by 0.1 μm within the agglomerate to evaluate their influence on the mechanical properties of the aerogels. These analyses showed that while the bond distribution affects the overall mechanical response, the differences in the uniaxial compression test results between different bond configurations were relatively small at the strain levels considered in our study. The values that exhibited the highest agreement with the experiments for the individual aerogels were used for the subsequent analysis of the aerogels packed beds.

The structural model for the BPM simulations was constructed based on μCT measurements obtained from previous work carried out by Dosta et al. [21] that also analyzed biopolymer aerogels containing 2 wt% alginate concentration. The authors demonstrated that cylindrical aerogel samples exhibit a slightly heterogeneous radial porosity distribution, as revealed by μCT imaging. However, we assumed a homogeneous porosity distribution for our simulations to simplify the model and obtain feasible simulation times. It is important to emphasize that aerogels' real microstructure, consisting of a fibrillar network with fibers in the order of magnitude of 10 nm (as also observed in Section 3.2), cannot be directly replicated using the BPM due to its inherent limitations. To address this, we represented the aerogel's foamed-like structure as an assembly of small primary particles interconnected by bonds. This approach maximizes the number of bonds while maintaining computational feasibility for the simulation analysis of packed beds. Although this simplified representation does not fully capture the fine-

scale microstructure, it is supported by experimental observations and offers a reasonable approximation of the aerogel's mechanical behavior under uniaxial compression. Additionally, it should be noted that the objective of this study is not to simulate the mechanical response of biopolymer gels at the microstructural level, which has already been comprehensively addressed in previous works [20,28,29]. Rather, the focus lies on investigating the macroscale mechanical behavior and characteristics in aerogel particle packed beds. The generated insights are intended to provide a basis for the systematic scale-up of the process to application-relevant production scales in future studies.

For the bed simulation, 100, 125, and 150 agglomerates were randomly placed in a steel mold with a 5 cm diameter and 2.5 cm height, ensuring no overlaps between agglomerates. After that, the generated agglomerates were set to fall, forming different compacted beds. To simplify the consequent fitting procedure, the bond model for these generation and settling stages was adjusted so that no breakage or plastic deformation could occur in bonds, making the agglomerates almost incompressible during these simulation stages. To assess the influence of agglomerate positioning during compaction, 10 distinct bed configurations were generated for each bed size, resulting in 10 unique beds for 100 agglomerates, 10 for 125 agglomerates, and 10 for 150 agglomerates.

2.2.2. Functional model

The contacts between particles, as well as between the particles and the rigid walls, were described by the Hertz-Mindlin model, a method extensively referenced in the literature and also applied by Dosta et al. [21,24,26]. The model considers the normal $\vec{F}_{n,pp}$ and tangential $\vec{F}_{t,pp}$ components of the force (Eq. (1)). The normal component (Eq. (2)) is represented by the Hertz model (Eq. (3)) [31] supplemented by an additional damping force proposed by Tsuji et al. (Eq. (4)) [32]:

$$\vec{F}_{pp} = \vec{F}_{n,pp} + \vec{F}_{t,pp}, \tag{1}$$

$$\vec{F}_{n,pp} = \vec{F}_{n,spring} + \vec{F}_{n,damping}, \tag{2}$$

$$\vec{F}_{n,spring} = -\frac{2}{3} k_n \xi_n \vec{r}_n, \tag{3}$$

$$\vec{F}_{n,damping} = -2\sqrt{\frac{5}{6}}\alpha \left|\vec{v}_{rel,n}\right| \sqrt{k_n m^*}\, \vec{r}_n. \tag{4}$$

Here, k_n is the particle stiffness in the normal direction (Eq. (5)); ξ_n is the overlap of particles in a normal direction; $\vec{r}_n$ is the normalized contact vector between the centers of the particles $\vec{P}_1$ and $\vec{P}_2$ (Eq. (6)); $\vec{v}_{rel,n}$ is the relative velocity of particles in a normal direction; m^* is the equivalent particle mass. The restitution coefficient between two particles is given by C_r, resulting in an α coefficient calculated as shown in Eq. (7):

$$k_n = 2E^* \sqrt{\xi_n r^*}, \tag{5}$$

$$\vec{r}_n = \frac{\vec{P}_1 - \vec{P}_2}{\left|\vec{P}_1 - \vec{P}_2\right|}, \tag{6}$$

$$\alpha = \frac{ln(C_r)}{\sqrt{\pi^2 + ln^2(C_r)}}, \tag{7}$$

where E^* is the equivalent Young's modulus of particles, and r^* is the equivalent particle radius.

Similarly, the total force in the tangential direction $\vec{F}_{t,pp}$ is calculated by Eq. (8) [33], considering the slipping condition:

$$\vec{F}_{t,pp} = \begin{cases} \vec{F}_{t,spring} + \vec{F}_{t,damping} & , \left|\vec{F}_{t,spring}\right| \le \mu_{sliding}\left|\vec{F}_{n,pp}\right| \\ \vec{F}_{t,spring}\mu_{sliding}\dfrac{\left|\vec{F}_{n,pp}\right|}{\vec{F}_{t,spring}} & , \left|\vec{F}_{t,spring}\right| > \mu_{sliding}\left|\vec{F}_{n,pp}\right| \end{cases}, \tag{8}$$

$$\vec{F}_{t,spring} = k_t \vec{\xi}_t, \tag{9}$$

$$\vec{F}_{t,damping} = -2\sqrt{\frac{5}{6}}\alpha \vec{v}_{rel,t} \sqrt{k_t m^*} \tag{10}$$

where $\mu_{sliding}$ is the sliding friction coefficient; k_t is the particle stiffness in the tangential direction (Eq. (11)); $\vec{v}_{rel,t}$ is the relative velocity of the particles in the tangential direction:

$$k_t = 8G^* \sqrt{\xi_n r^*}. \tag{11}$$

Here, G^* is the equivalent shear modulus. The tangential overlap $\vec{\xi}_t$ in the current step is calculated iteratively considering its previous value $\vec{\xi}_{t,prev}$ (Eqs. (12) and (13)). The tangential overlap to be applied in the following iteration $\vec{\xi}^{\,t+\Delta t}_{t,prev}$, is transformed depending on the slipping condition (Eq. (14)):

$$\vec{\xi}_t = \vec{v}_{rel,t}\Delta t + \vec{\kappa}\frac{\left|\vec{\xi}_{t,prev}\right|}{\left|\vec{\kappa}\right|}, \tag{12}$$

$$\vec{\kappa} = \vec{\xi}_{t,prev} - \vec{r}_n\left(\vec{r}_n \bullet \vec{\xi}_{t,prev}\right), \tag{13}$$

$$\vec{\xi}^{\,t+\Delta t}_{t,prev} = \begin{cases} \vec{\xi}_t & , \left|\vec{F}_{t,spring}\right| \le \mu_{sliding}\left|\vec{F}_{n,pp}\right| \\ \dfrac{\vec{F}_{t,pp}}{k_t} & , \left|\vec{F}_{t,spring}\right| > \mu_{sliding}\left|\vec{F}_{n,pp}\right| \end{cases}, \tag{14}$$

Here, Δt is the simulation time step.

For the calculation of rotational moments, the rotational velocity of particles $\vec{\omega}$ and the coefficient of the rolling friction $\mu_{rolling}$ is considered:

$$\vec{M}_{pp} = \vec{r}_n \times \vec{F}_{t,pp} r + \tau, \tag{15}$$

$$\tau = -\mu_{rolling} r \left|\vec{F}_{n,spring}\right| \frac{\vec{\omega}}{\left|\vec{\omega}\right|}, \tag{16}$$

where r is the particle radius, and τ is the rolling torque.

The bond model proposed by Dosta et al. [21] was applied. The model was derived using a linear elastic beam model to calculate the tangential forces and moments. In contrast, the normal force was determined by accounting for the elasto-plastic behavior of the material. Separate methods were applied to handle tension and compaction during the calculations. Fig. 3 illustrates the schematic stress-strain curves for a single bond under various loading conditions according to the model by Dosta et al. [21]:

The model starts as a classical linear elastic beam with stiffness defined as follows:

$$k_{n,b} = \frac{E_b A_b}{l_b} \tag{17}$$

$$k_{t,b} = \frac{E_b}{2l_b(1-\nu_b)} \tag{18}$$

Here, l_b is the initial length of the bond, A_b is its cross-sectional area and ν_b is the Poisson's ratio of the bonds. When the bond breaks at the

compressive yield strain ε_y, the normal force gradually decreases by $\beta k_{n,b}$, until it reaches zero. The bond remains in the simulation but is regarded as quasi-broken after this point. The plastic deformation of the bond occurs with additional compaction. However, according to the particle-particle interaction model, the bonded particles can still transmit forces if they come into contact.

Tensile stress acts on the bond when it undergoes tensile loading once more, implying interlocking within the structure. The stiffness of the bond in this tensile regime is $\alpha k_{n,b}$, meaning that unloading instantly produces a tensile force.

In the simulation analysis, the preliminary investigation focused on the uniaxial compaction of a single aerogel at a piston speed of 3 mm/s. As a starting point, the values proposed by Dosta et al. [21] for the model parameters and functional model for primary particles were applied according to Table 1. To find suitable Young's moduli for the primary particles and bonds, their values were incrementally modified by 50 kPa, starting from 100 kPa. The results between experiments and simulations were compared using the R^2 value. The obtained values for the material properties were then used in the analysis with slower piston velocity for validation.

The obtained values of the Young's moduli were then applied to simulate the packed beds. In order to find the suitable particle and bond model parameters while minimizing the simulation time, automatic optimization of the simulation values was applied using the developed coupling between MATLAB [34] and the MUSEN framework. The force-displacement curves generated from the simulations were compared to the experiments, and the resulting R^2 value was used as an input for the nonlinear programming solver *fminsearch,* which is based on a simple search method proposed by Lagarias et al. [35] that presented reduced simulation times in previous investigations [36].

The packed beds consisting of 100, 125, and 150 particles exhibited average heights of 13.77 mm, 15.87 mm, and 17.97 mm, respectively, reflecting the differing particle counts. To achieve a consistent strain deformation of 90 % across all beds, the required model times were 4.8 s, 5.4 s, and 6.0 s, respectively. The simulation time step varied according to Young's modulus rather than fixed at the smallest acceptable value to improve the efficiency of the simulations. Once the best agreement was achieved, a convergence analysis was performed to determine the appropriate time step.

The average computational time for a single uniaxial compaction simulation of the alginate aerogels particle packed bed samples consisting of 100 particles (69,000 primary particles and 265,000 bonds) was approximately 1 h on a computer with Intel Xeon Gold 5118 CPU and NVIDIA Quadro GV100 GPU. For the beds of 125 particles (86,250 primary particles and 331,875 bonds) and 150 particles (102,120 primary particles and 392,940 bonds), the simulation times increased to **6.1 h** and 8.5 h, accordingly, with the same applied computer.

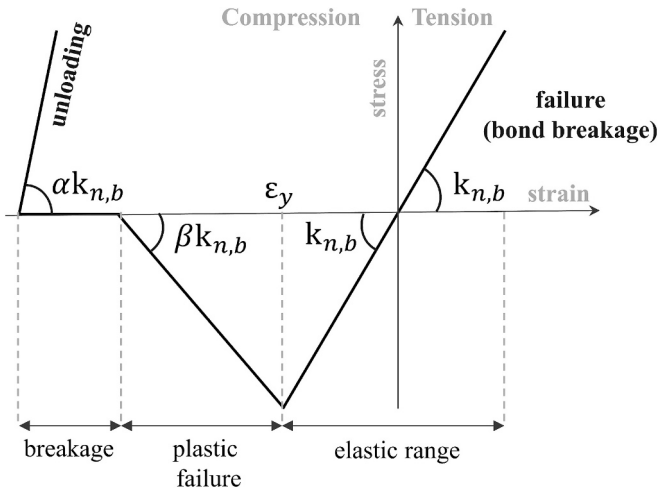

Fig. 3. Schematic stress-strain curve for a solid bond subjected to normal loading according to the bond model by Dosta et al. [21].

3. Results and discussion

To investigate the mechanical properties of alginate aerogels both as individual particles and within packed beds, uniaxial compaction experiments were conducted, complemented by DEM-BPM simulations (schematics shown in Fig. 2). In the first part of this study, the textural and physical properties of the alginate aerogel particles were analyzed (section 3.1), while in the second part, these samples were utilized for the calibration and validation of the DEM-BPM simulations (section 3.2).

3.1. Properties of the alginate aerogel particles

The alginate-based aerogel particles investigated in this study are shown in Fig. 4a. They are colorless, have a circularity of 0.96 ± 0.02 and an average particle diameter of 3.28 ± 0.01 mm. The corresponding cumulative (Q_0) and narrow density distributions (q_0) of 50 aerogel particles show that particles are highly uniform (Fig. 3b). The corresponding median particle size (D_{50}) is 3.26 mm, and overall sizes vary only slightly within a 3.13 to 3.44 mm range. The bulk density of the particle beds was determined to be 0.047 ± 0.005 g/cm^3.

Microstructural characterization via nitrogen physisorption yielded typical type IV isotherms (H3 shape, see Fig. S1 b), which verify the mesoporous nature of the produced aerogels and point toward the additional presence of macropores [30]. The specific surface area of 352 ± 16 m^2/g (estimated on linear BET plot, see Fig. S1 a) was within the typical range for alginate aerogels (~ 350 to 570 m^2/g) [37–40]. This also accounts for the mesopore volume (1.67 ± 0.49 cm^3/g) and mean pore diameter (14.14 ± 6.18 nm) (derived from pore size distributions, see Fig. S1 c), which were in the expected range, even though the mean pore diameter is on the lower end [38,39].

Fig. 4c shows the obtained SEM image of the corresponding inner aerogel microstructure (magnification = 50,000×). Results from nitrogen physisorption are confirmed by SEM images of the inner pore structure, which show an open meso- to macroporous fibrillar structure, which is typical for biopolymer aerogels.

The mechanical behavior of aerogel particles was investigated via uniaxial compaction tests (20 repetitions for each experiment). The averaged data is displayed in Fig. 4d, the individual measurements can be seen in Fig. S2. The experiments were performed with two distinct compaction velocities of the probe and a stopping condition of 100 N. The lines in Fig. 4 b and d are drawn to guide the eye, and the hatched areas represent the standard deviation of the average data.

Strain-stress curves of biopolymer aerogels are typically divided into three main regions: I) a linear range, II) a plateau characterized by pore collapse, and III) a range of further densification [19,20]. However, due to the changing contact area between the gel particle and the probe during compaction, only force-displacement curves, rather than stress-

Table 1
Model and material parameters for single aerogel simulations applied as starting point, based on Dosta et al. [21].

Bond model parameters	
Compressive yield strain (ε_y) [%]	3.52
Plastic failure (β) [−]	−0.3
Interlocking stiffness factor (α)[−]	30
Material parameters	
Poisson ratio [−]	0.2
Friction coefficient [−]	0.1
Rolling friction [−]	0.05

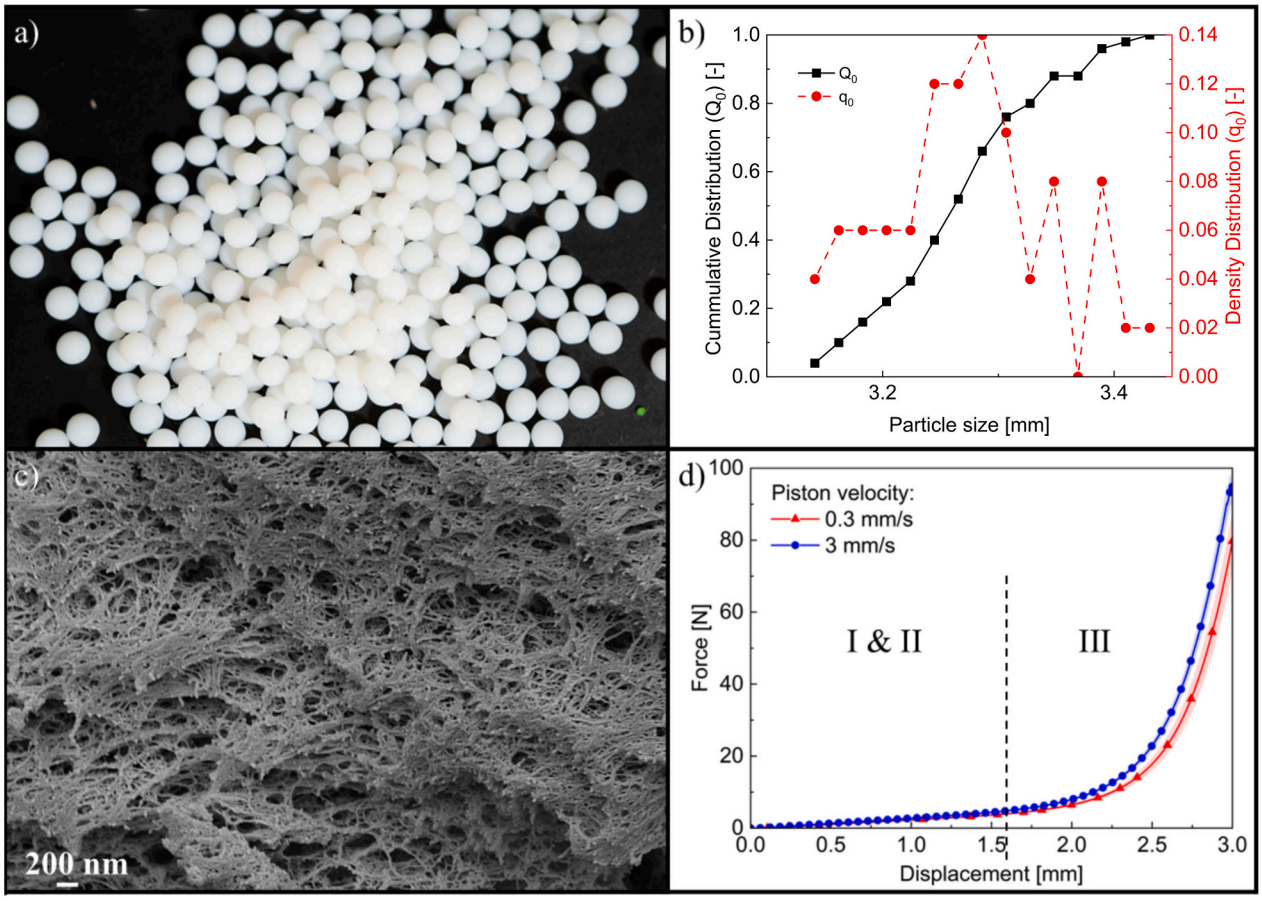

Fig. 4. Characterization of 2 wt% alginate particles used to perform uniaxial compaction tests: a) Particle shape, b) Particle size distribution, c) SEM image of the corresponding inner aerogel microstructure, d) Force-displacement curves of uniaxial compaction tests.

strain curves, can be obtained for individual particle experiments. Despite this limitation, distinct phases were identified in the case of alginate aerogel particles investigated in this study. However, the transition between the linear region and the plateau is less pronounced compared to monolithic samples, as noted in the study by Dosta et al. [21]. Normally, the linear phase extends from the beginning of the curve

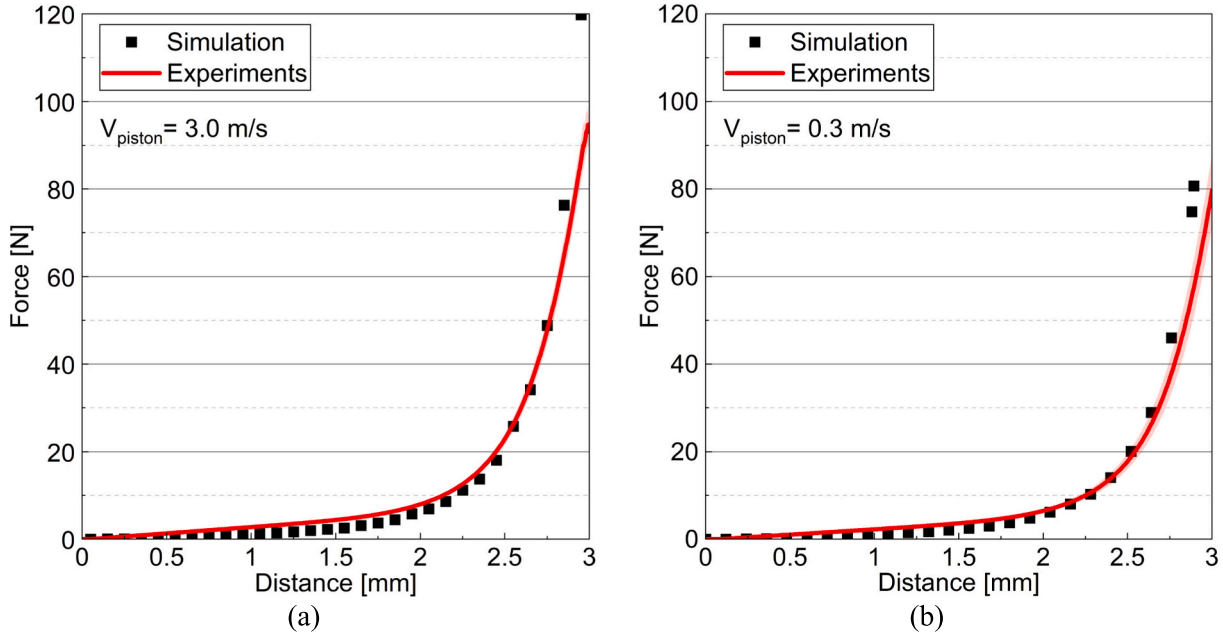

Fig. 5. Comparison between averaged experiments and simulations for the uniaxial compaction of alginate aerogels (2 wt%) with a probe velocity of (a) 3 mm/s and (b) 0.3 mm/s.

up to 5–8 % strain for biopolymer aerogel monolith, while for the particles investigated in this study, no precise distinction can be made between the linear phase and the plateau [20 – 22]. Nevertheless, the third phase is categorized based on a linear fit through the first two phases, and a decreasing R^2 below 0.999 is defined as the criterion for identification. At this point, the phase of network densification begins (R^2 = 0.9977 for 0.3 mm/s and R^2 = 0.9982 for 3 mm/s).

It is evident that increasing the compaction velocity from 0.3 mm/s by a factor of 10 results in an increase in the compressive strength of the aerogel particles. This behavior is likely due to the reduced relaxation time of the biopolymer network at higher velocities, limiting its ability to respond to applied forces from the probe.

3.2. Simulation characterization and aerogel packed bed compaction

The first part of the simulation analysis investigates the compaction behavior of individual alginate aerogel particles, serving as a calibration step for DEM-BPM simulations. Following this, the study explores the behavior of these particles in packed beds of 100 to 150 aerogel particles.

3.2.1. Simulation of single aerogel compaction

In the subsequent part of this study, the single-particle compaction tests serve as the calibration foundation for the DEM-BPM simulations. Fig. 5a and Fig. 5b show the comparison of experiments and simulations with the best agreement for the uniaxial compaction of single aerogels at 3 mm/s and 0.3 mm/s, respectively.

The uniaxial compaction experiments at 3 mm/s showed the highest agreement with the simulations, with an R^2 value of 0.95. The error bars in the simulations represent the standard deviation calculated from the results of the 10 independently generated packed bed configurations for each particle count. This accounts for the variability in initial packing structures and their influence on the compaction behavior. The material and simulation parameters used to achieve this agreement are listed in Table 2.

Applying these parameters for simulating uniaxial compaction at 0.3 mm/s resulted in an R^2 value of 0.93. The strong agreement observed in both simulation cases confirms the validity of the proposed bond model for describing the mechanical behavior of aerogels, both as monoliths (observed by Dosta et al. [21]) and as particles. The simulation time step was set to $5e^{-8}$ s based on a previous analysis of convergence and a recommended time step provided by MUSEN [41].

When comparing the compaction force levels achieved at varying piston velocities, it was observed that faster compaction of aerogel particles resulted in higher force levels. This behavior can be attributed to the shorter relaxation time of the gel structures at higher velocities. The rapid application of force allows the gel structure to absorb more energy before plastic deformation or failure occurs, resulting in a stiffer response. Regarding the simulation, the absence of particle-particle interactions for pairs of particles directly connected by bonds in single-particle compaction ensures that the observed behavior reflects the material's inherent strain rate sensitivity rather than being influenced by inter-particle forces. Consequently, the model parameters for the simulation, particularly the interlocking stiffness factor, play a crucial role in capturing this strain rate sensitivity and accurately simulating the mechanical response.

Table 2
Bond model parameters and material parameters for single particle compaction.

Bond model parameters	
Compressive yield strain (ε_y) [%]	3.52
Plastic failure (β) [−]	−0.9
Interlocking stiffness factor (α) [−]	30
Material parameters	
Poisson ratio [−]	0.2
Friction coefficient [−]	0.4
Rolling friction [−]	0.2
Bond Young's Modulus [MPa]	4.00
Particle Young's Modulus [MPa]	5.00

The greatest discrepancies between experiments and simulations occur at higher deformation levels, which can be attributed to the limitations inherent in the simulation assumptions. Key assumptions include the lack of deformability of the primary particles. Additionally, aerogels often exhibit nonlinear mechanical behaviors at higher deformation levels, such as plastic deformation or structural collapse, which are challenging to fully replicate in simulations, particularly when the model assumes simplified material properties like a constant Young's modulus [21,42]. The calibrated Young's modulus values of the bonds and particles obtained in this initial analysis were used to simulate the aerogel beds.

Fig. 6 illustrates the stress distribution within the bonds of a single aerogel particle and how it evolves with piston displacement.

The data presented in the matrices represents the evolution of bond counts over time under different applied stress levels. At time $t = 0$, bonds are first only present at the lowest stress level at both compaction velocities; bonds are absent at all other stress levels. As time passes, bonds progressively move to higher stress levels during the compaction with slower prove velocity, suggesting a regulated deformation and stress redistribution process. For a probe velocity of 0.3 mm/s, the bond count gradually declines as tension rises, indicating a steady yet slow bond breaking under increased stress. The nonlinear mechanical response of this process is probably caused by differences in material behavior or local stress concentrations. The bond counts gradually level off at lower numbers, indicating a shift. As plastic deformation advances, the bond counts gradually settle at lower levels, indicating a shift toward structural breakdown or a steady-state situation. A small portion of the material can sustain tremendous loads before failing completely, as seen by the occurrence of distributed low bond counts at high stresses.

In comparison, a very distinct pattern can be observed during compaction at a probe velocity of 3 mm/s. The bond count declines dramatically within the first fraction of piston displacement, with bonds breaking down quickly at all stress levels. By 0.06 mm piston displacements, the bond count has already dropped significantly, and by 2.5 mm, it has reached zero, indicating that the material has experienced quick and severe bond breakage. This implies that quick compaction uses a considerably larger energy or force in a shorter time period, resulting in an accelerated deformation process. The quick decrease in bond count indicates that the material encounters broad stress concentrations and bond failure practically immediately, providing little opportunity for stress redistribution or structural adjustment. The absence of bonds at later time periods suggests that the material experienced total structural breakdown significantly earlier than in the compaction with slower probe velocity. As a result, whereas both compaction analyses begin with an identical starting bond distribution, their reactions to stress and deformation are significantly different.

Slow compaction exhibits a gradual, controlled process with a nonlinear mechanical response, leading to a more stable but eventual structural failure. On the other hand, fast compaction results in rapid and widespread bond breakage, leading to almost immediate structural failure. These distinctions highlight the trade-off between stability and speed in compaction processes, with slow compaction promoting controlled deformation and quick compaction prioritizing rapid material consolidation at the expense of structural integrity. This analysis is also evident in the maximum agglomerate deformability for both probe velocities compaction (Fig. 7a and Fig. 7b). These findings are also consistent with experimental results where higher particle strength was observed at higher compression rates.

3.2.2. Simulation of packed aerogel bed compaction

Fig. 8 shows the comparison between experiments and optimized

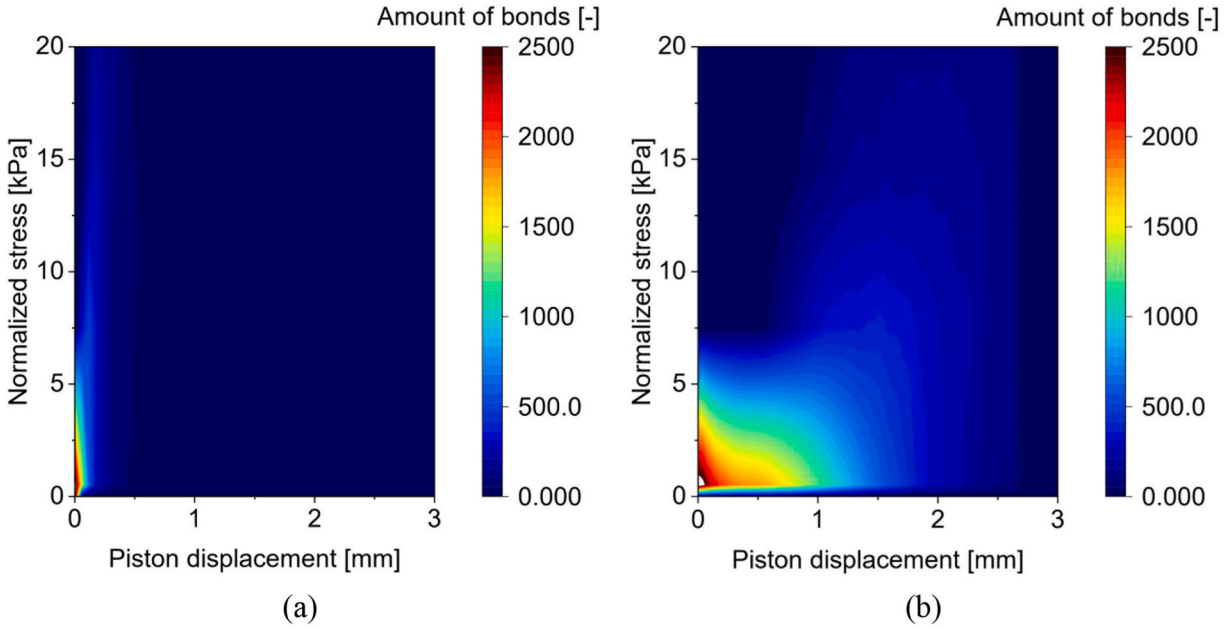

Fig. 6. Stress distribution within the 2656 bonds of a single aerogel particle during uniaxial compaction with probe velocity of (a) 3 mm/s and (b) 0.3 mm/s.

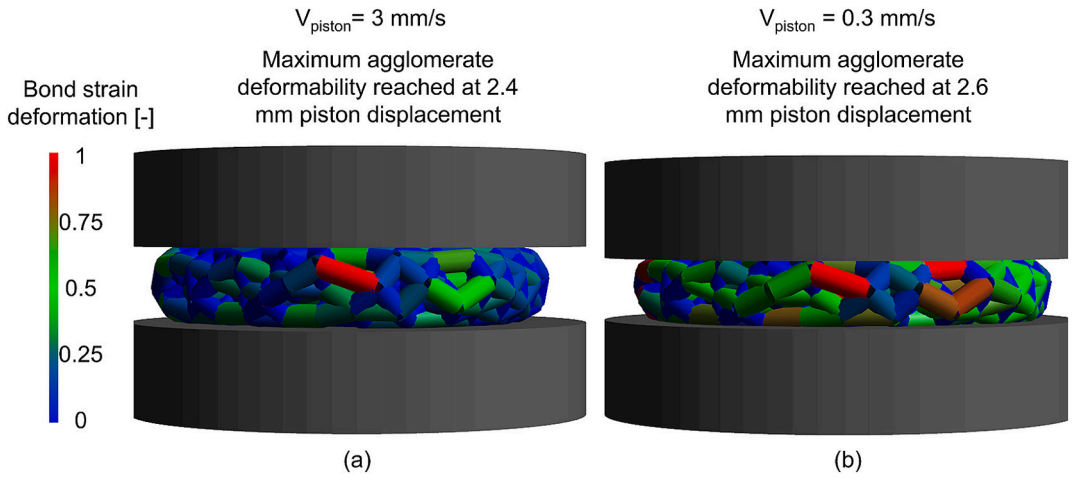

Fig. 7. Qualitative analysis of simulated agglomerate deformation under probe velocity compaction at (a) 3 mm/s and (b) 0.3 mm/s.

simulations for the compaction of alginate aerogels bed of 100, 125, and 150 particles, respectively:

A strong correlation was observed for all particle beds, with R^2 values of 0.97, 0.94, and 0.93 for the beds containing 100, 125, and 150 particles, respectively. The optimized values utilized for the simulations can be seen in Table 3:

A higher interlocking stiffness factor is observed, which can be attributed to the more complex and diverse interactions of aerogels with multiple neighboring particles. These interactions create greater resistance to deformation, reflected as increased interlocking stiffness in the model. In packed beds, the applied load is shared among multiple agglomerates and their bonds, enhancing the system's overall stiffness as bonds work collectively to resist deformation more effectively than in single-particle systems [43]. Furthermore, the packed configuration introduces constraints due to the surrounding particles, limiting the ability of individual particles to deform freely and resulting in an apparent increase in stiffness. Higher friction values are also noted, which aligns with expectations since packed beds exhibit additional contact forces and friction between agglomerates that are not present in single-agglomerate simulations [44,45]. These additional forces further resist movement, contributing to the elevated interlocking stiffness factor.

The simulation typically converged after an average of 40 iterations. As a result, the optimization analysis for the 100-particle bed required approximately 52.6 h on average. The optimized parameters shown in Table 3 were then utilized to simulate beds of different sizes to reduce computational time. This proposed optimization methodology for DEM model parameters proves to be more efficient than the traditional trial-and-error approach commonly used for calibration, which is often time-intensive, sometimes reaching months [46]. In this context, MUSEN [41] stands out as an appealing tool for DEM simulation due to its high computational efficiency, which is achieved through GPU support, parallel computing capabilities, and the ability to integrate with external software packages, thereby streamlining the optimization process.

Comparatively, the deviations observed between different experimental trials for each bed size are significantly smaller than those among the various simulated agglomerate configurations. In the experimental setup, the packed bed height for 100 aerogels ranged from 9.2 mm to 11.8 mm, with a standard deviation of 0.6 mm, highlighting considerable variability in the initial packing structure. For the 125-particle bed,

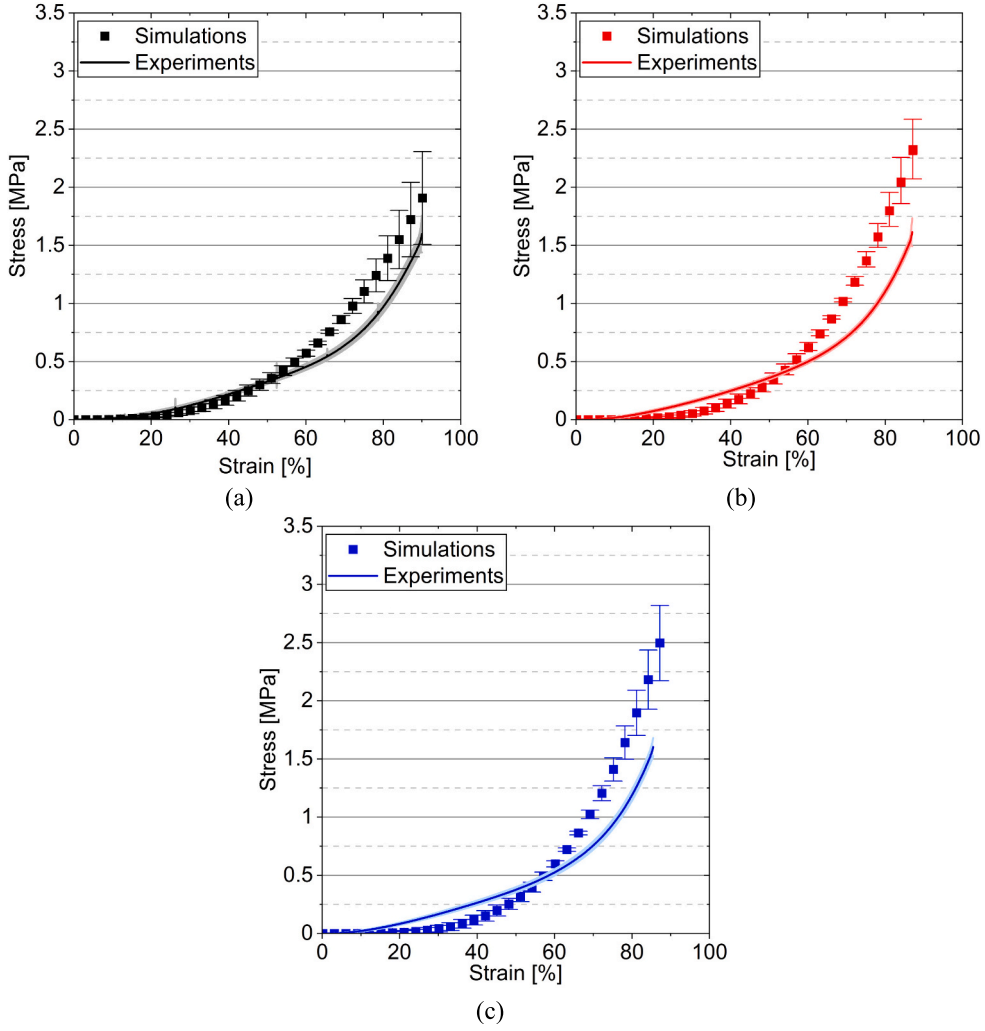

Fig. 8. Comparison of experimental and simulation results for the uniaxial compaction of 2 % alginate concentration aerogels in beds composed of (a) 100 particles, (b) 125 particles, (c) 150 particles.

Table 3
Optimized values of bond model parameters and material parameters for the simulation of aerogel beds.

Bond model parameters	
Compressive yield strain (ε_y) [%]	3.52
Plastic failure (β) [−]	−1
Interlocking stiffness factor (α) [−]	35
Material parameters	
Poisson ratio [−]	0.2
Friction coefficient [−]	0.5
Rolling friction [−]	0.045
Bond Young's Modulus [MPa]	4.00
Particle Young's Modulus [MPa]	5.00

these values are from 13.0 mm to 15.4 mm, with a similar standard deviation of 0.6 mm. The 150-particle bed exhibited a range of 14.4 mm to 16.8 mm, with a slightly higher standard deviation of 0.9 mm. This variability results from natural differences in particle arrangements and procedural inconsistencies during bed preparation. Therefore, the initial height of the packings were used to calculate the strain from the raw displacement data (Fig. 8c). The varying packing height therefore has only a minor influence on the presented experimental data (force-distance curve for 150 particles is given in Fig. S4). Given that the aerogel particles under analysis are biopolymer-based, the variability of the biopolymer composition and the variations during production such as the particle size also affect the batch-to-batch reproducibility of the experimental results. These variations lead to higher deviations compared to single batch replicates as shown in Fig. 8. To emphasize these deviations, two distinct batches of 150 particles in a packed bed under uniaxial compression (with 20 repetitions) are compared and shown in Fig. S5.

In contrast, the numerical simulations assumed incompressible agglomerates during the generation and settling phases with no breakage or plastic deformation allowed. This assumption was made to reduce computational complexity, avoid introducing plastic deformation effects, and ensure structural stability, allowing the focus to remain on tracking the deformability of the agglomerates during uniaxial compaction. As a result, the simulated packed beds exhibited greater uniformity compared to the experimental results. The simulated 100-particle beds ranged from 13.2 mm to 13.7 mm, with a standard deviation of 0.4 mm. Similarly, the 125-particle beds ranged from 18.4 mm to 18.8 mm, with a standard deviation of 0.3 mm, and the 150-particle beds ranged from 23.1 mm to 23.4 mm, with a standard deviation of 0.2 mm. This assumption of relative incompressibility of the agglomerates may explain the underestimation of stresses in simulations at lower strains since the modeled particles might have slightly lower internal stresses during the initial compression stages than the experimental samples.

On the other hand, at higher strains, the overestimation of stresses can be explained by a combination of several mechanisms. One factor is

the assumption that direct particle-particle contact forces are disabled for particles directly connected by bonds. As the deformation progresses, more initially distant particles come into contact. The breakage of the bonds additionally contributes to this increase in the number of particle-particle contacts. This increases the number of additional force transmission paths, thereby amplifying the overall stress response. In parallel, the incompressibility of the primary particles prevents local deformation and energy dissipation, leading to an unrealistically stiff behavior at large strains. Furthermore, as the strain increases, aerogels typically undergo a collapse of their internal pore network, which is currently not captured by the model. Microstructural deformations (e.g., slight plasticity) and interparticle friction in real aerogels mitigate sharp force fluctuations, stabilize force chains, and reduce abrupt variations in stress transmission, acting as damping and energy dissipation mechanisms [43,44,47].

Moreover, accounting for the initial deformability of aerogel particles during bed construction in experiments could explain why larger particle counts result in greater deformation and, consequently, higher discrepancies with the idealized simulations. In contrast, the numerical model lacks these dissipation effects, making it more prone to oscillations and force fluctuations. This absence can amplify deviations in force measurements between simulation runs, even under similar initial conditions. As the number of aerogels in the packed bed increases, small variations in local contact forces accumulate, leading to larger discrepancies between simulations and experiments. In experiments, external boundary conditions, interparticle adhesion, and friction naturally regulate these variations, whereas in simulations, numerical discrepancies propagate more freely as system size grows.

The most effective approach for simulating the scale-up process would involve utilizing mesoscale simulations, such as FEM, to capture the macroscopic behavior of the system. FEM is particularly well-suited for modeling aerogels at the micro level, including the biopolymer network and micromechanics. This macroscopic information could then be transferred to the microscale to assess its influence on individual gel particles, providing a comprehensive understanding of the interactions and effects across scales. The highest discrepancy can be observed after 70 % strain deformation. Similarly, there is a higher variability among the simulations of the beds with the same particle counts. These observed variabilities can be attributed to many different factors. Because of random initialization, every simulated packed bed has a distinct particle arrangement, which causes changes in the distribution of stress and the patterns of deformation as strain increases. Differences between simulations become more noticeable at higher strain levels because even slight variations in initial configurations or particle interactions are amplified. Furthermore, increased deformation exacerbates localized effects that differ between beds and increase variability, such as particle collapse or uneven load distribution [26].

The simulation framework may not adequately represent the more intricate particle interactions that result from higher strain, such as friction, rearrangement, or crushing. Similar to single particle analysis, the aerogel particles may experience nonlinear mechanical behavior at greater strains, including plastic deformation, densification, and structural collapse, all of which are challenging to simulate using simplistic simulation models. The assumption of non-compressible primary particles is directly linked to the overestimation of the compaction stress of the simulations compared to the experiments.

Considering the inherent heterogeneity in the alginate composition and aerogels structure that results from their manufacture, a greater deviation was anticipated when comparing the experiment runs. However, as evidenced by the average deviations of 14.7 %, 8.7 %, and 19.9 % for the 100, 125, and 150 particle beds, respectively, the large number of aerogel particles in the bed statistically covers this compositional variation. Notably, this variability is also effectively captured by the simulations, demonstrating their ability to replicate the experimental behavior.

Considering that even minor differences in single-particle properties can significantly impact the results, a greater deviation might have been anticipated when comparing the experimental runs for packed beds. However, as evidenced by the average deviations of 14.7 %, 8.7 %, and 19.9 % for the 100, 125, and 150 particle beds, respectively, the experimental results demonstrate good homogeneity and reproducibility of the samples, likely due to the consistent production procedure and uniform starting materials (see standard deviation in Fig. 4). While the simulations capture this variability to some extent, the observed deviations are influenced by model simplifications, such as the absence of stickiness in the contact models and friction areas, which highlight areas for potential optimization.

4. Conclusion

This study presents the first mechanical analysis of aerogel particles in a packed bed. The alginate aerogel investigated is a highly open-porous solid material with a specific surface area of 352 m^2/g. The particles (circularity of 0.96) exhibit a narrow size distribution with an average diameter of 3.28 mm.

Given the growing demand for (bio)polymer aerogels, attributed to their unique properties and diverse applications, it is necessary to scale up the current state-of-the-art production processes in packed bed systems. However, such scaling introduces higher mechanical stress on the particle bed. In order to replicate these forces, uniaxial compaction tests were performed on individual particles as well as packed beds containing 100, 125, and 150 particles, providing insights into the underlying deformation mechanisms.

The proposed DEM-BPM accurately reproduced and predicted the mechanical behavior of alginate aerogels, demonstrating strong agreement between simulations and experiments, with minor deviations ($R^2 \geq 0.93$ for all cases). The discrepancies observed in packed bed simulations at high compressive strengths can be attributed to the random initial packing structure, localized stress redistributions, progressive failure of bonds, incompressibility of the primary particles, and increased influence of the particle-particle contacts, leading to variations in the compaction response. Moreover, the pre-deformation of the agglomerates during the filling process—an aspect not explicitly considered in this simulation—could further influence the compaction behavior, particularly at lower strains. Future studies should incorporate a more detailed characterization of agglomerate deformation prior to compaction and introduce consideration of microstructural deformations and collapses, which may provide additional insights into stress redistribution and mechanical stability during large-scale processing.

Overall, this study highlights the potential of the DEM-BPM model approach not only for the mechanical characterization of aerogels in packed beds but also as a valuable tool to support the scale-up process of aerogel production by predicting the deformation processes. Future model enhancements could include particle-fluid interactions, enabling the characterization of intermediate products such as hydrogels and alcogels during aerogel manufacturing.

Supplementary data to this article can be found online at https://doi.org/10.1016/j.powtec.2025.121048.

CRediT authorship contribution statement

C.L. Alves: Writing – review & editing, Writing – original draft, Visualization, Validation, Project administration, Methodology, Investigation, Formal analysis, Data curation, Conceptualization. **L. Gibowsky:** Writing – original draft, Visualization, Investigation, Data curation. **B. Schroeter:** Writing – review & editing, Supervision, Resources. **I. Smirnova:** Writing – review & editing, Supervision, Project administration, Funding acquisition. **S. Heinrich:** Writing – review & editing, Supervision, Project administration, Funding acquisition.

Declaration of competing interest

The authors declare that they have no known competing financial interests or personal relationships that could have appeared to influence the work reported in this paper.

Acknowledgments

We gratefully acknowledge the financial support of the DFG Graduate School GRK 2462 “Processes in Natural and Technical Particle Fluid Systems (PintPFS)” (Project No. 390794421).

The alginate sample was kindly provided by IFF Nutrition & Health Germany GmbH & Co KG, Walsrode- Bomlitz (IFF Division Pharma Solutions).

Data availability

Data will be made available on request.

References

[1] I. Smirnova, P. Gurikov, Aerogel production: current status, research directions, and future opportunities, J. Supercrit. Fluids 134 (2018) 228–233.
[2] I. Smirnova, P. Gurikov, Aerogels in chemical engineering: strategies toward tailor-made aerogels, Annu. Rev. Chem. Biomol. Eng. 8 (2017) 307–334.
[3] N. Gaponik, A.-K. Herrmann, A. Eychmüller, Colloidal nanocrystal-based gels and aerogels: material aspects and application perspectives, J. Phys. Chem. Lett. 3 (2012) 8–17.
[4] E. Cuce, P.M. Cuce, C.J. Wood, S.B. Riffat, Toward aerogel based thermal superinsulation in buildings: a comprehensive review, Renew. Sust. Energ. Rev. 34 (2014) 273–299.
[5] M. Betz, C.A. García-González, R.P. Subrahmanyam, I. Smirnova, U. Kulozik, Preparation of novel whey protein-based aerogels as drug carriers for life science applications, J. Supercrit. Fluids 72 (2012) 111–119.
[6] M. Martins, A.A. Barros, S. Quraishi, P. Gurikov, S.P. Raman, I. Smirnova, A.R. C. Duarte, R.L. Reis, Preparation of macroporous alginate-based aerogels for biomedical applications, J. Supercrit. Fluids 106 (2015) 152–159.
[7] International Union of Pure and Applied Chemistry, IUPAC Announces the 2022 Top Ten Emerging Technologies in Chemistry. https://iupac.org/iupac-2022-top-ten/, 2022. Accessed 20 January 2025.
[8] R. Subrahmanyam, P. Gurikov, I. Meissner, I. Smirnova, Preparation of biopolymer aerogels using green solvent, J. Vis. Exp. 113 (2025) e54116.
[9] T. Ahmad, F.A. Masoodi, S.A. Rather, S.M. Wani, A. Gull, JBCC 5 (1) (2019) 114–122.
[10] S.R. Comim, K. Madella, J.V. Oliveira, S.R.S. Ferreira, Supercritical fluid extraction from dried banana peel (Musa spp., genomic group AAB): extraction yield, mathematical modeling, economical analysis and phase equilibria, J. Supercrit. Fluids 54 (2010) 30–37.
[11] T. Budtova, Cellulose II aerogels: a review, Cellulose 26 (2019) 81–121.
[12] M.A. Aegerter, N. Leventis, M. Koebel, S.A. Steiner III (Eds.), Springer Handbook of Aerogels, Springer International Publishing, Cham, 2023.
[13] I. Selmer, Prozessoptimierung der überkritischen Trocknung von Proteinaerogelen und deren Anwendung im Lebensmittelbereich, 2021.
[14] S. Zhao, W.J. Malfait, N. Guerrero-Alburquerque, M.M. Koebel, G. Nyström, Biopolymer aerogels and foams: chemistry, properties, and applications, Angew. Chem. Int. Ed. Eng. 57 (2018) 7580–7608.
[15] A. Giuma, H.P.S.A. Khalil, E.B. Yahya, L. Sukeksi, T. Alfatah, N.M. Nurazzi, M. Jaber, I. Surya, Green thermal insulators: a review into the role of biopolymer-based aerogels in thermal insulation applications, Polym. Eng. Sci. 64 (2024) 4611–4629.
[16] B. Schroeter, P. Jeansathawong, A. Hajnal, P. Gurikov, Wet milling of alginate Alco- and hydrogel composites: a facile top-down approach for continuous production of aerogel microparticles, Macro Mater. Eng. 308 (2023).
[17] B. Merillas, C.A. García-González, T.E.G. Álvarez-Arenas, M.Á. Rodríguez-Pérez, Towards the optimization of polyurethane Aerogel properties by densification: exploring the structure–properties relationship, Small Struct. 5 (2024).
[18] S.F. Plappert, J.-M. Nedelec, H. Rennhofer, H.C. Lichtenegger, F.W. Liebner, Strain hardening and pore size harmonization by uniaxial densification: a facile approach toward superinsulating aerogels from Nematic Nanofibrillated 2,3-Dicarboxyl cellulose, Chem. Mater. 29 (2017) 6630–6641.
[19] I. Karadagli, B. Schulz, M. Schestakow, B. Milow, T. Gries, L. Ratke, Production of porous cellulose aerogel fibers by an extrusion process, J. Supercrit. Fluids 106 (2015) 105–114.
[20] A. Rege, M. Schestakow, I. Karadagli, L. Ratke, M. Itskov, Micro-mechanical modelling of cellulose aerogels from molten salt hydrates, Soft Matter 12 (2016) 7079–7088.
[21] M. Dosta, K. Jarolin, P. Gurikov, Modelling of mechanical behavior of biopolymer alginate aerogels using the bonded-particle model, Molecules (Basel, Switzerland) 24 (2019).
[22] D.O. Potyondy, P.A. Cundall, A bonded-particle model for rock, Int. J. Rock Mech. Min. Sci. 41 (2004) 1329–1364.
[23] M. Nitka, J. Tejchman, Modelling of concrete behaviour in uniaxial compression and tension with DEM, Granul. Matter 17 (2015) 145–164.
[24] S. Rybczynski, G. Schaan, M. Dosta, M. Ritter, F. Schmidt-Döhl, Discrete element modeling and electron microscopy investigation of fatigue-induced microstructural changes in ultra-high-performance concrete, Materials (Basel, Switzerland) 14 (2021).
[25] H. Wu, J. Zhao, N. Guo, Multiscale insights into borehole instabilities in high-porosity sandstones, JGR Solid Earth 123 (2018) 3450–3473.
[26] C.L. Alves, V. Skorych, A. de Noni, D. Hotza, S.G. González, S. Heinrich, Microscale DEM simulation of spray-dried porcelain granules under uniaxial compaction, Powder Technol. 428 (2023) 118863.
[27] K. Ganesan, T. Budtova, L. Ratke, P. Gurikov, V. Baudron, I. Preibisch, P. Niemeyer, I. Smirnova, B. Milow, Review on the production of polysaccharide aerogel particles, Materials (Basel, Switzerland) 11 (2018).
[28] P.N. Depta, P. Gurikov, B. Schroeter, A. Forgács, J. Kalmár, G. Paul, L. Marchese, S. Heinrich, M. Dosta, DEM-based approach for the modeling of gelation and its application to alginate, J. Chem. Inf. Model. 62 (1) (2022) 49–70.
[29] R. Chandrasekaran, M. Hillgärtner, K. Ganesan, B. Milow, M. Itskov, A. Rege, Computational design of biopolymer aerogels and predictive modelling of their nanostructure and mechanical behaviour, Sci. Rep. 11 (2021) 10198.
[30] M. Thommes, K. Kaneko, A.V. Neimark, J.P. Olivier, F. Rodriguez-Reinoso, J. Rouquerol, K.S.W. Sing, Physisorption of gases, with special reference to the evaluation of surface area and pore size distribution (IUPAC technical report), Pure Appl. Chem. 87 (2015) 1051–1069.
[31] H. Hertz, Ueber die Berührung fester Elastischer Körper, Crll 1882, 1882, pp. 156–171.
[32] Y. Tsuji, T. Tanaka, T. Ishida, Lagrangian numerical simulation of plug flow of cohesionless particles in a horizontal pipe, Powder Technol. 71 (1992) 239–250.
[33] R.D. Mindlin, H. Deresiewicz, Elastic spheres in contact under varying oblique forces, J. Appl. Mech. 20 (1953) 327–344.
[34] The MathWorks Inc, MATLAB Version: 9.13.0 (R2023b), The MathWorks Inc, Natick, Massachusetts, United States, 2023. https://www.mathworks.com.
[35] J.C. Lagarias, J.A. Reeds, M.H. Wright, P.E. Wright, Convergence properties of the nelder–mead simplex method in low dimensions, SIAM J. Optim. 9 (1998) 112–147.
[36] C.L. Alves, V. Skorych, A. de Noni, D. Hotza, S.Y. Gómez González, S. Heinrich, M. Dosta, Improving the sustainability of porcelain tile manufacture by flowsheet simulation, Ceram. Int. 49 (2023) 24581–24597.
[37] T. Duong, M. Vivero-Lopez, I. Ardao, C. Alvarez-Lorenzo, A. Forgács, J. Kalmár, C. A. García-González, Alginate aerogels by spray gelation for enhanced pulmonary delivery and solubilization of beclomethasone dipropionate, Chem. Eng. J. 485 (2024) 149849.
[38] A. Veronovski, Z. Novak, Ž. Knez, Synthesis and use of organic biodegradable aerogels as drug carriers, J. Biomater. Sci. Polym. Ed. 23 (2012) 873–886.
[39] F. Quignard, R. Valentin, F. Di Renzo, Aerogel materials from marine polysaccharides, New J. Chem. 32 (2008) 1300.
[40] M. Robitzer, L. David, C. Rochas, F. Di Renzo, F. Quignard, Nanostructure of calcium alginate aerogels obtained from multistep solvent exchange route, Langmuir ACS J. Surf. Coll. 24 (2008) 12547–12552.
[41] M. Dosta, V. Skorych, MUSEN: an open-source framework for GPU-accelerated DEM simulations, SoftwareX 12 (2020) 100618.
[42] N. Buchtová, C. Pradille, J.-L. Bouvard, T. Budtova, Mechanical properties of cellulose aerogels and cryogels, Soft Matter 15 (2019) 7901–7908.
[43] M. Dosta, C. Costa, H. Al-Qureshi, Numerical investigation of compaction of deformable particles with bonded-particle model, EPJ Web Conf. 140 (2017) 15021.
[44] B. Harthong, J.-F. Jérier, P. Dorémus, D. Imbault, F.-V. Donzé, Modeling of high-density compaction of granular materials by the discrete element method, Int. J. Solids Struct. 46 (2009) 3357–3364.
[45] Y. Guo, Q. Chen, Y. Xia, J. Klinger, V. Thompson, A nonlinear elasto-plastic bond model for the discrete element modeling of woody biomass particles, Powder Technol. 385 (2021) 557–571.
[46] C. Coetzee, A. Katterfeld, Calibration of DEM parameters, in: D. McGlinchey (Ed.), Simulations in Bulk Solids Handling, Wiley, 2023, pp. 1–40.
[47] M.P. Dirauf, A. Hajnal, P. Gurikov, A.S. Braeuer, Protein gel shrinkage during solvent exchange: quantification of gel compaction, mass transfer and compressive strength, Food Hydrocoll. 120 (2021) 106916.